Research Article Vol. 33, No. 13 / 30 Jun 2025 / *Optics Express* 28679

Optics EXPRESS

Analytic ray tracing model and MATLAB code for GRIN rod lens imaging probe design

JIN YOUNG YOUM[1,2] **AND JOON-MO YANG**[1,*]

[1] *Center for Photoacoustic Medical Instruments, Department of Biomedical Engineering, Ulsan National Institute of Science and Technology (UNIST), Ulsan 44919, Republic of Korea*
[2] *Current Address: Department of Radiological Science, Nambu University, Gwangju 62271, Republic of Korea*
[*] *jmyang@unist.ac.kr*

Abstract: Achieving an accurate working distance in gradient index (GRIN) rod lens–based miniaturized imaging probes is critical for the successful implementation of imaging systems in various biophotonic applications. Although numerous commercial optical design software tools are available for such designs and simulations, they are often too expensive for typical research laboratories and require substantial time and effort for beginners to learn and use effectively. In this paper, we present a simple yet practically useful MATLAB-based simulation code and an underlying ray tracing model. Our approach is based on the principle that the trajectory of an optical ray entering a GRIN lens medium is deterministically defined by the boundary conditions at the entrance surface. We evaluated the accuracy of the developed model using a typical optical fiber and GRIN lens configuration commonly employed in miniaturized imaging probes. Notably, for the assumed probe configuration where a paraxial approximation is valid, the predicted working distances closely matched the results obtained from commercial software. Given that many laboratories lacking access to specialized software have had to rely solely on manufacturer feedback to determine the specifications of a GRIN lens—often at the cost of considerable time—this model could serve as a valuable alternative to facilitate progress in related research.

1. Introduction

Gradient index (GRIN) lenses have been widely utilized in various biophotonic applications, such as optical coherence tomography [1–6], confocal microscopy [7–10], two-photon microscopy [11,12], and photoacoustic imaging [13–24], in addition to their conventional use in optical communication systems where probe miniaturization is a core requirement. Due to the critical role of GRIN lens optics, numerous studies have introduced models capable of solving the complex ray equation [Eq. (1)] [25], even under the assumption of a general GRIN lens medium with an arbitrary refractive index distribution $n(x,y,z)$ [26–46], such as spherical [43], planar [44], and eccentric [39] distributions—in the ray equation [Eq. (1)], ds represents the differential length along the ray trajectory and $\vec{r}(s) \equiv (x(s), y(s), z(s))$. However, researchers focused on practical imaging system implementation—especially in biophotonics—often lack the time to delve into such sophisticated theoretical models. Instead, they typically need a straightforward method to determine the GRIN lens pitch for focusing at a desired working distance or to predict and verify the working distance using existing commercial GRIN rod lenses. The term "GRIN rod lens" here refers to a lens with a cylindrical shape and a refractive index distribution that varies only with the radial distance from its axis, $n(r)$, and is independent of the axial coordinate z, along which rays propagate. For GRIN rod lenses typically utilized in biophotonics, the radial refractive index distribution $n(r)$ is known to follow a nearly parabolic profile, as described by Eq. (2), where n_0 represents the refractive index at the center, r denotes the radial distance, and g denotes the gradient constant. For simplicity, we hereinafter refer to the GRIN rod lens simply as

#564584
Journal © 2025
https://doi.org/10.1364/OE.564584
Received 8 Apr 2025; revised 8 Jun 2025; accepted 10 Jun 2025; published 27 Jun 2025

a "GRIN lens."

$$\frac{d}{ds}\left(n\frac{d\vec{r}(s)}{ds}\right) = \nabla n \tag{1}$$

$$n(r) = n_0(1 - \frac{1}{2}g^2r^2) \tag{2}$$

Commercial optical design software packages such as Zemax, 3DOptix, Code V, and COMSOL offer solutions for accurately computing ray trajectories using proprietary algorithms. However, beyond the considerable time and cost required, a fundamental limitation is that the accuracy of these simulations heavily depends on the number of parameters used to define the refractive index distribution n(r). In practice, GRIN lens manufacturers typically provide only two parameters: n_0, the refractive index at the lens center, and g, the gradient constant.

In this context, a study by Jung *et al.* proposed a practically valuable modeling method for designing GRIN lens-based miniaturized imaging probes from the perspective of wave optics or beam optics, offering useful guidelines for related research [2]. In brief, the authors presented a method to calculate the working distance and corresponding beam diameter based on analytical formulas derived in closed form, and also discussed how variations in input parameters affect outcomes such as beam diameter and working distance. However, since the model is based on 2×2 ray-transfer matrices, also known as the ABCD matrix, for optical systems composed of multiple serially connected media, the resulting formulas are structurally complex. Additionally, the accuracy of the calculated results may be lower than that of commercial optical design software, as the ray-transfer matrix approach inherently relies on paraxial approximations. Moreover, it does not generate ray-tracing diagrams that allow for immediate visual interpretation of the simulated ray trajectories.

Acknowledging both the inaccessibility of expensive commercial software and the limitations of existing modeling approaches, we sought to develop a new GRIN lens probe design model that is freely accessible to standard laboratories and grounded in ray optics. This led to the creation of a MATLAB-based simulation code and ray tracing model capable of generating visual representations of ray trajectories using analytical solutions derived from the paraxial ray equation.

The remainder of this paper is structured as follows. It begins with a brief overview of GRIN lens optics, outlines the assumptions and parameter definitions underlying our modeled optical system, introduces our modeling concept and the associated MATLAB implementation, and concludes with validation results and an example in vivo image acquired using a probe designed via this model.

2. Basic principles and formulas for GRIN lens

Due to the unique refractive index distribution of a GRIN lens, as defined by Eq. (2) and depicted in Fig. 1(a), any paraxial ray originating from a point within the lens medium follows a sinusoidal trajectory with a period of $2\pi/g$, as shown in Fig. 1(b). Owing to this characteristic behavior, such rays are often referred to as cosine rays, and in this discussion, we restrict our analysis to rays propagating within meridional planes. Here, it should be noted that the parameter g, which determines the sinusoidal period, is the same parameter used to describe the radial refractive index profile in Eq. (2). This is because for the paraxial rays confined to the y-z plane, as defined in Fig. 1(b), the general ray equation [Eq. (1)] simplifies under the paraxial approximation to Eq. (3), whose solutions are known to be harmonic functions [25].

$$\frac{d^2y}{dz^2} = -g^2y \tag{3}$$

Thus, if an object, represented by an arrow, is positioned at the entrance or first surface of a GRIN lens [Fig. 1(b)], an image of identical size can be formed at a location one full pitch length

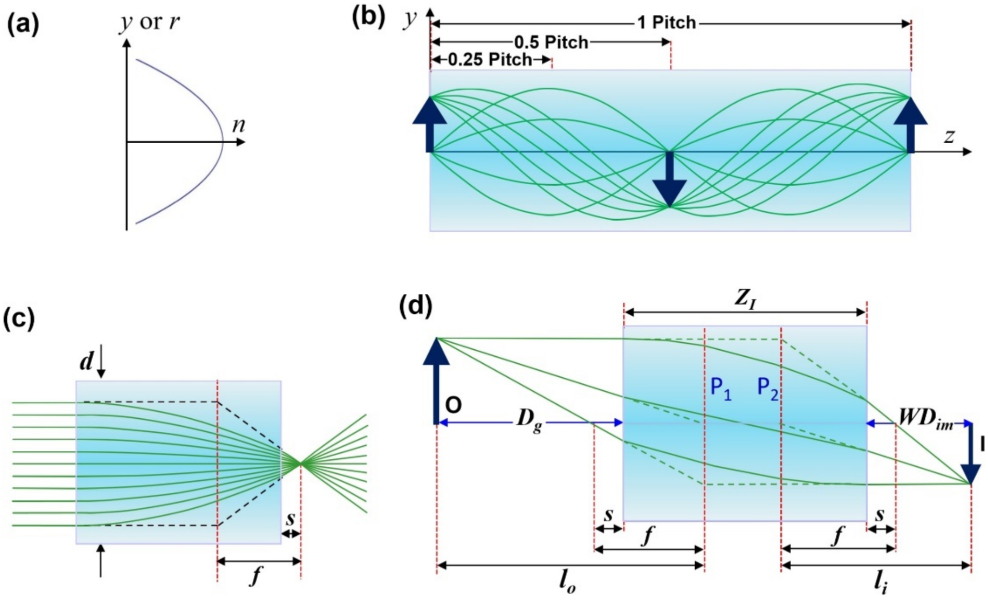

Fig. 1. Physical and optical characteristics of the GRIN lens. (a) Radial refractive index distribution of a GRIN lens. (b) Ray trajectories in a GRIN lens with one pitch. (c) Definition of the back focal length (f) and working distance (s) of a GRIN lens with a pitch value of 0.25. (d) Illustration showing the image formation principle in a GRIN lens. Here, P1 and P2 indicate the principal points.

(Z_{1P}) away. This is because an ideal GRIN lens is designed so that all rays originating from a single point on the object reconverge after completing one sinusoidal cycle, corresponding to the pitch length. Thus, a GRIN lens with a pitch of 1 (or 2, 3, etc.) will reproduce the object placed at its entrance surface identically at the exit surface. The pitch length (Z_{1P}) is related to the gradient constant (g) by the following equation:

$$\mathrm{Z}_{1P} = \frac{2\pi}{g} \tag{4}$$

where the subscript “1P” represents one pitch. While Eq. (3) describes this particular case, practical scenarios often involve GRIN lenses with lengths that do not correspond exactly to a full pitch. To address this, a parameter known as the “characteristic pitch” (P) is introduced. Then, the physical length (Z_I) of a given lens can then be expressed in terms of this pitch as follows:

$$\mathrm{Z}_I = \frac{2\pi}{g}P \tag{5}$$

In miniaturized imaging probes typically implemented in biophotonics—such as endoscopic systems—the GRIN lens typically has a pitch value of less than 0.25. In these cases, the primary function of the lens is not to relay an image, as shown in Fig. 1(b), but to focus a laser beam emitted from a guiding optical fiber to a specific working distance. When $P < 0.25$, parallel rays originating from an object at infinity are focused at a point beyond the rear (second) surface of the GRIN lens, as illustrated in Fig. 1(c). Depending on whether the distance is measured from the second principal plane or from the rear surface, the former is called the back focal length and the latter the working distance, and the corresponding back focal length (f) and working distance

(s) can be approximately calculated using Eqs. (6) and (7).

$$f = \frac{1}{n_0 g \sin(gZ_I)} = \frac{1}{n_0 g \sin(2\pi P)} \tag{6}$$

$$s = \frac{1}{n_0 g \tan(gZ_I)} = \frac{1}{n_0 g \tan(2\pi P)} \tag{7}$$

Here, it should be noted that the back focal length f and working distance s are intrinsic properties of a GRIN lens, determined by the refractive index n_0 and the gradient constant g. Thus, the working distance s should be clearly distinguished from another parameter, WD_{im}, which is also called a working distance in this paper but is defined as the distance from the rear surface of the GRIN lens to the image formed when the object is positioned a distance D_g away from the lens entrance, as shown in the general case depicted in Fig. 1(d). That is, the working distance WD_{im} is not an intrinsic parameter defined by the specifications of a GRIN lens like the case of s, but a kind of dependent variable introduced to define the distance to the image from the rear surface for an arbitrary location of an object. Here, D_g refers to the gap between the optical fiber tip and the entrance surface of the GRIN lens, which we refer to as the "gap distance"—with the subscript 'g' indicating "gap." The subscript '*im'* in WD_{im} stands for "immersion medium," because the image space may be filled with air or a liquid such as water or oil.

Using Eqs. (6) and (7), the location of the image (l_i) for an object placed at a distance (l_o) from the lens can be determined by substituting into the thin lens equation, as expressed in Eq. (8).

$$\frac{1}{l_o} + \frac{1}{l_i} = \frac{1}{f} \tag{8}$$

It should be noted that l_o and l_i represent distances measured from the two principal points indicated in Fig. 1(d), not from the physical surfaces of the lens. Therefore, by re-expressing Eq. (8) in terms of the parameters D_g and WD_{im}, we obtain Eq. (9):

$$\frac{1}{D_g + f - s} + \frac{1}{WD_{im} + f - s} = \frac{1}{f} \tag{9}$$

Substituting Eqs. (6) and (7) into Eq. (9) for the back focal length (f) and working distance (s), and rearranging the terms, we derive the following expression:

$$\tan(gZ_I) = \tan(2\pi P) = \frac{n_0 g(D_g + WD_{im})}{n_0^2 g^2 D_g WD_{im} - 1} \tag{10}$$

Solving Eq. (10) for Z_I or P yields Eq. (11):

$$gZ_I = 2\pi P = \tan^{-1}\left(\frac{n_0 g(D_g + WD_{im})}{n_0^2 g^2 D_g WD_{im} - 1}\right) \tag{11}$$

This equation is particularly useful for calculating the required physical length (Z_I) or pitch (P) of a GRIN lens given specific values of n_0, g, D_g, and WD_{im} or for predicting the working distance WD_{im} when n_0, g, D_g, and P are known.

It should be emphasized, however, that the results obtained from Eqs. (10) and (11) are approximate, as their derivation involves paraxial approximations. Nonetheless, these equations are valuable for providing an initial estimate of the working distance WD_{im}, which can then be refined using the iterative forward prediction method implemented in our MATLAB simulation code, to be presented in Section 4. In this approach, the initial estimate serves as a starting point, from which a more accurate value can be determined through successive iterations.

3. GRIN lens optics system to be modeled

Before introducing our modeling concept, it is essential to first define the optical system under consideration. For this purpose, we refer to the optical fiber–GRIN lens–right-angle prism configuration that has been employed in our optical-resolution photoacoustic endoscopic probes, as reported in our previous studies [21,22]. A typical configuration of the probes is illustrated in Fig. 2(a). Because the probes were designed to achieve high-resolution imaging, the primary objective is to form a tightly focused optical beam at a specific working distance.

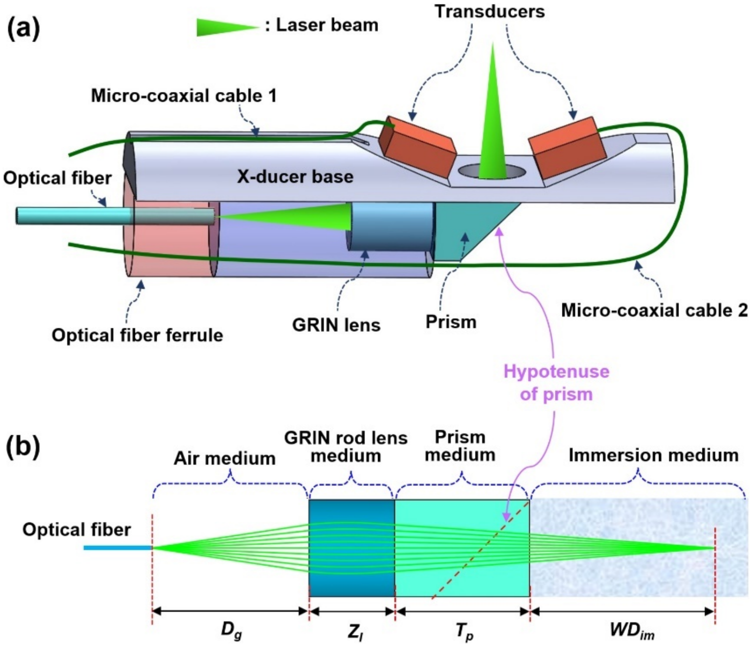

Fig. 2. Schematic of the photoacoustic endoscopic probe set as a modeling target. (a) Optical fiber–GRIN lens–right-angle prism configuration employed in our optical-resolution photoacoustic endoscopic probes [21,22]. (b) Equivalent optical system of (a).

To briefly describe the laser beam trajectory: the laser pulse emitted from the optical fiber initially propagates through air over a distance D_g, then enters the GRIN lens, and is finally focused at the intended working distance (WD_{im}), after passing through the prism and immersion mediums. The tightly focused beam then generates photoacoustic waves through the photoacoustic effect—details of which can be found in Refs. 21 and 22. In this optical system, the prism merely functions to redirect the exiting laser beam from the GRIN lens toward a lateral direction.

Accordingly, this optical system can be simplified to its equivalent model shown in Fig. 2(b), where the prism is represented as a slab medium of thickness T_p, and all relevant modeling parameters are clearly defined for further discussion.

While many miniaturized imaging probes employed in other optical imaging applications [1–12] do not incorporate a prism component, we adopt this slightly more complex system in our model. This is because those types of probes also can be modeled by simply removing the prism medium or treating it as part of the immersion medium, which may consist of air or a liquid such as water or oil.

4. Ray tracing model developed in this study

As discussed in Section 2, for a GRIN lens defined by specific parameters n_0, g, and P, the image location can be calculated using Eq. (11). However, because the equation is derived from the thin lens approximation and expressed in a closed-form solution, it does not provide any insight into the detailed trajectories of individual rays.

However, if we note the fact that all paraxial rays within a GRIN lens follow sinusoidal paths—due to the harmonic nature of the solutions to the paraxial ray equation [Eq. (3)]—it can be observed that the only additional information required to determine the trajectory function of each ray are the boundary conditions. In other words, the subsequent trajectory of any optical ray entering the GRIN lens can be deterministically derived solely from the boundary conditions at the entrance surface. Consequently, the trajectory function of each ray can also be expressed in a closed-form solution.

To illustrate our modeling concept more precisely, first we introduce a Cartesian coordinate system onto the optical configuration shown in Fig. 2(b), as depicted in Fig. 3(a). We consider the case where a paraxial ray is emitted from the tip of an optical fiber at a non-zero launch angle θ_1, propagating along the trajectory represented by the green curve. Here, we only consider paraxial rays confined to meridional planes that originate from a single point, as the primary objective of this model is to predict the optical working distance based on a set of given optical and geometrical parameters. Figure 3(b) presents the corresponding 2D representation of the ray trajectory along with the definitions of the parameters used in the model.

Importantly, in the xyz-coordinate system defined in Figs. 3(a) and 3(b), the origin is chosen such that the z-axis aligns with the optical axis of the GRIN lens and the peak of the cosine ray coincides with the y-axis. This configuration enables any cosine ray trajectory within the GRIN lens medium to be represented by the simple closed-form function $f(z)=a\cdot\cos(gz)$, where a represents an amplitude and g represents the given gradient constant. For a paraxial ray entering the GRIN lens with an incident angle θ_1 and an initial y-position y_{b1}, as depicted in Fig. 3(b), the task is now reduced to determining only the amplitude a. This is straightforward, as the y-coordinate of the cosine ray at the entrance surface must match the value y_{b1} by the boundary condition. Additionally, the refraction angle θ_2, which determines the slope of the cosine ray at the entry point, can be obtained using Snell's law. Consequently, for the entrance surface, the following relationships can be derived based on the two boundary conditions: matching the y-coordinate and the slope at the point of entry.

$$n_a \sin\theta_1 = n\left(y_{b1}\right)\sin\theta_2, \text{ by Snell's law} \tag{12}$$

$$y_{b1} = f(-Z_{I1}) = a\cos(gZ_{I1}), \text{ by the } y\text{-coordinate value} \tag{13}$$

$$\tan\theta_2 = \left.\frac{df(z)}{dz}\right|_{z=-Z_{I1}} = ag\sin(gZ_{I1}), \text{ by the slope} \tag{14}$$

Using Eq. (12), the refraction angle θ_2 can be readily calculated for a given incident angle θ_1 and local refractive index $n(y_{b1})$, as defined by Eq. (2). Once θ_2 is known, the amplitude a of the cosine ray can be determined using Eq. (15), which is derived by substituting Eqs. (13) and (14) into the general identity $\cos^2\alpha + \sin^2\alpha = 1$ (valid for any α).

$$a = \sqrt{\frac{\tan^2\theta_2}{g^2} + y_{b1}^2} \tag{15}$$

With the amplitude a determined, the key parameter defining the cosine ray in a closed-form expression has now been fully resolved. Subsequently, the value of Z_{I1} can be obtained by

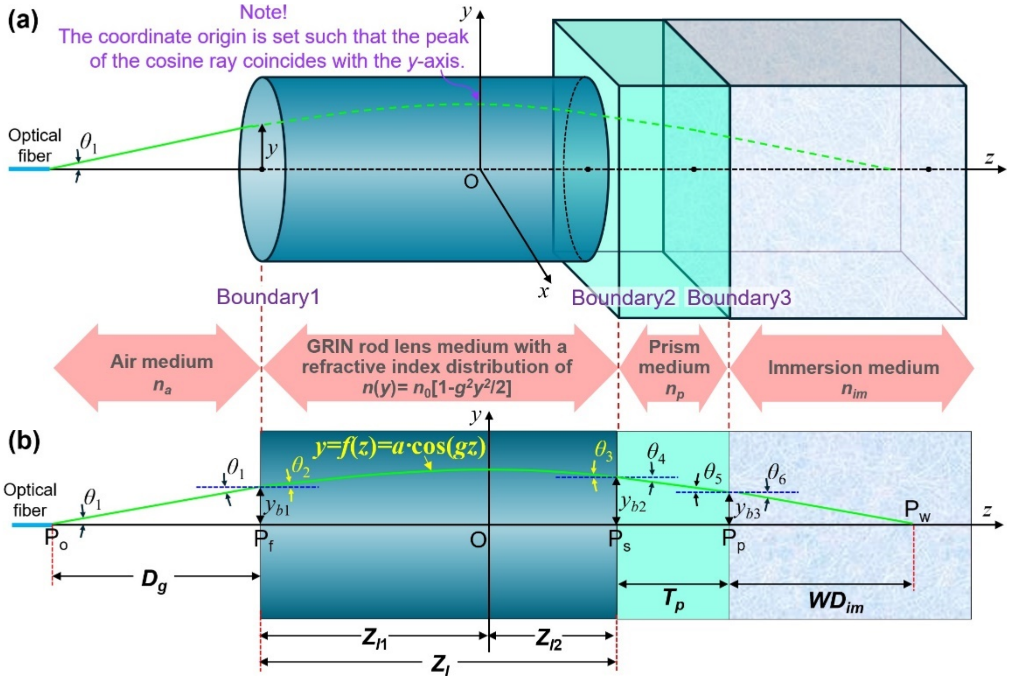

Fig. 3. Schematic of the modeled optical system. (a) Optical system to be modeled with an overlaid Cartesian coordinate system. (b) Corresponding 2D optical layout illustrating the ray trajectory from (a) and the parameters defined for the modeling. In (a), the coordinate origin is set such that the z-axis aligns with the optical axis of the GRIN lens, and the peak of the cosine ray coincides with the y-axis. Accordingly, in (b), the GRIN lens is divided into two sections, Z_{I1} and Z_{I2}, representing the ascending and descending sections of the cosine ray described by $f(z)=a\cdot\cos(gz)$. The model considers only rays emitted from the optical fiber tip at a non-zero launch angle θ_1, within the numerical aperture of the fiber, and propagating along meridional planes.

substituting Eq. (15) into Eq. (13), and can be expressed as Eq. (16).

$$Z_{I1} = \frac{\cos^{-1}(y_{b1}/a)}{g} \tag{16}$$

Here, Z_{I1} denotes the length of the rising section of the cosine ray according to the aforementioned setting criterion for the y-axis, and thus the length of the descending section is simply given by $Z_{I2}= Z_I - Z_{I1.}$

With the descending segment length now established, the remaining ray trajectory through the prism and immersion mediums can be readily determined. Specifically, the y-position, y_{b2}, and exit angle θ_3 of the ray at Boundary2 can be calculated using the following Eqs. (17) and (18), respectively.

$$y_{b2} = f(Z_{I1}) = a\cos[g(Z_I - Z_{I1})] \tag{17}$$

$$\tan\theta_3 = -\left.\frac{df(z)}{dz}\right|_{z=-Z_{I2}} = ag\sin(gZ_{I2}),\ \text{by the slope at Boundary2} \tag{18}$$

Subsequently, the angle θ_4 can be determined by reapplying Snell's law at Boundary2, as shown below:

$$n(y_{b2})\sin\theta_3 = n_p\sin\theta_4 \tag{19}$$

$$\theta_4 = \sin^{-1}\left[\frac{n(y_{b2})\sin\theta_3}{n_p}\right] \tag{20}$$

With θ_4 now calculated from Eq. (20), and given that the ray propagates linearly through the prism medium, the corresponding y-position y_{b3} can be calculated using Eq. (21), as follows:

$$y_{b3} = y_{b2} - T_p\tan\theta_4,\ \text{where}\ \theta_4>0 \tag{21}$$

Moreover, because the ray propagates linearly within the prism, θ_5 is equal to θ_4. Therefore, the refraction angle θ_6 at Boundary3 can be obtained by applying Snell's law again:

$$\theta_6 = \sin^{-1}\left[\frac{n_p\sin\theta_5}{n_{im}}\right] \tag{22}$$

Finally, the working distance WD_{im} can be calculated using the following Eq. (23).

$$WD_{im} = y_{b3}/\tan(\theta_6),\ \text{where}\ y_{b3}>0 \tag{23}$$

It is important to note that if the thickness of the prism medium T_p is sufficiently large, the ray may intersect the optical axis before entering the immersion medium. Thus, before evaluating WD_{im}, the sign of y_{b3} obtained from Eq. (21) must be verified.

Through the procedure outlined above, the full trajectory of a paraxial ray can be analytically determined. This result is significant because it implies that, for the parameter set defined in Fig. 3(b), the complete ray trajectory can be described in a fully closed mathematical form across all propagation media.

5. MATLAB code and test result

Following the modeling approach described in Section 4, we also implemented a numerical calculation code (see Code 1 [51]) using commercial MATLAB software. In this implementation, the notations presented in Table 1 were adopted to represent parameters and variables—this was necessary due to MATLAB's limitations on allowable characters and symbols for variable names. In addition to the parameters defined in Section 4, the MATLAB code includes several additional variables, such as \`Num_Ray\` (the number of rays to be launched toward the upper half-plane), \`NAfiber\` (the numerical aperture of the optical fiber), and \`*d*\` (the diameter of the GRIN lens).

Based on the parameter definitions provided in Table 1 and the specific values listed in Table 2, we validated our model by comparing the optical working distance (WD_{im}) predicted by our model with the result obtained from a commercial optical design software, Zemax, as provided by the manufacturer. Notably, the gradient constant g, the refractive index at the center of the GRIN lens n_0, and the refractive index of the prism medium n_p, as listed in Table 2, are typically wavelength-dependent. Therefore, it is essential to ensure that the values used for these parameters correspond accurately to the specific wavelength applied in the imaging probe.

Figures 4 and 5 present the corresponding ray tracing results, where the NAfiber value for the simulations was commonly assumed to be 0.1 because that is a typical numerical aperture of the optical fibers being applied to miniaturized imaging probes in biophotonics.

First, as shown in the ray tracing diagrams in Fig. 4, the working distance (WD_{im}) of 2.13 mm calculated by our model [Fig. 4(b)] shows excellent agreement with the value computed by the GRIN lens manufacturer using Zemax [Fig. 4(a)]. Notably, the value of 2.13 mm was the target working distance that we initially specified and provided to the manufacturer.

Regarding the ray tracing parameters listed in Table 2, some were predetermined by us, while others were finalized by the GRIN lens manufacturer based on our specifications for the GRIN lens used in the photoacoustic mini-probe reported in Refs. 21 and 22. Specifically, dimensional parameters such as the GRIN lens diameter (0.5 mm), prism thickness ($T_p = 0.7$ mm), gap

Table 1. Notations of parameters and variables utilized in the MATLAB code implementation

Notation in the MATLAB code	Corresponding notation in Section 4	Type	Note
g	g	Parameter	Gradient constant of a GRIN lens [mm^{-1}]
n0	n_0	Parameter	Refractive index at the center of a GRIN lens
Ny	$n(y)$	Variable	Local refractive index of a GRIN lens at position y
na	n_a	Parameter	Refractive index of an air medium
np	n_p	Parameter	Refractive index of a prism medium
nim	n_{im}	Parameter	Refractive index of an immersion medium
Dg	D_g	Parameter	Gap distance between the fiber tip and GRIN lens [mm]
Tp	T_p	Parameter	Thickness of the prism medium [mm]
ZI	Z_I	Parameter	Geometrical (or physical) length of a GRIN lens [mm]
ZI1	Z_{I1}	Variable	Physical length of the GRIN lens section over which a cosine ray ascends
ZI2	Z_{I2}	Variable	Physical length of the GRIN lens section over which a cosine ray descends
Amp	a	Variable	Amplitude of a cosine ray as utilized in Eq. (13)
WDim	WD_{im}	Variable	Working distance or z-intercept created by a ray [mm]
ang1	θ_1	Variable	Launched angle of a paraxial ray with respect to the z-axis
ang2	θ_2	Variable	Angle of refraction of a paraxial ray at Boundary1
ang3	θ_3	Variable	Incident angle of a paraxial ray at Boundary2
ang4	θ_4	Variable	Angle of refraction of a paraxial ray at Boundary2
ang5	θ_5	Variable	Incident angle of a paraxial ray at Boundary3
ang6	θ_6	Variable	Angle of refraction of a paraxial ray at Boundary3
Yb1	y_{b1}	Variable	y-coordinate value of a ray at Boundary1
Yb2	y_{b2}	Variable	y-coordinate value of a ray at Boundary2
Yb3	y_{b3}	Variable	y-coordinate value of a ray at Boundary3

Table 2. Parameter set used for ray trajectory calculations in the MATLAB code (Code 1)

Parameters according to Section 4	Corresponding notation in the MATLAB code	Applied value	Note
g	g	1.382 mm^{-1} @ 532 nm	Provided by the manufacturer
n_0	n0	1.635 @ 532 nm	Provided by the manufacturer
-	d	0.5 mm	Reflected in our request
n_a	na	1.0	Reflected in our request
n_p	np	1.51958 @ 532 nm	Reflected in our request
n_{im}	nim	1.33	Reflected in our request
D_g	Dg	1.06 mm	Reflected in our request
T_p	Tp	0.7 mm	Reflected in our request
Z_I	ZI	0.44 mm	Finalized by the manufacturer

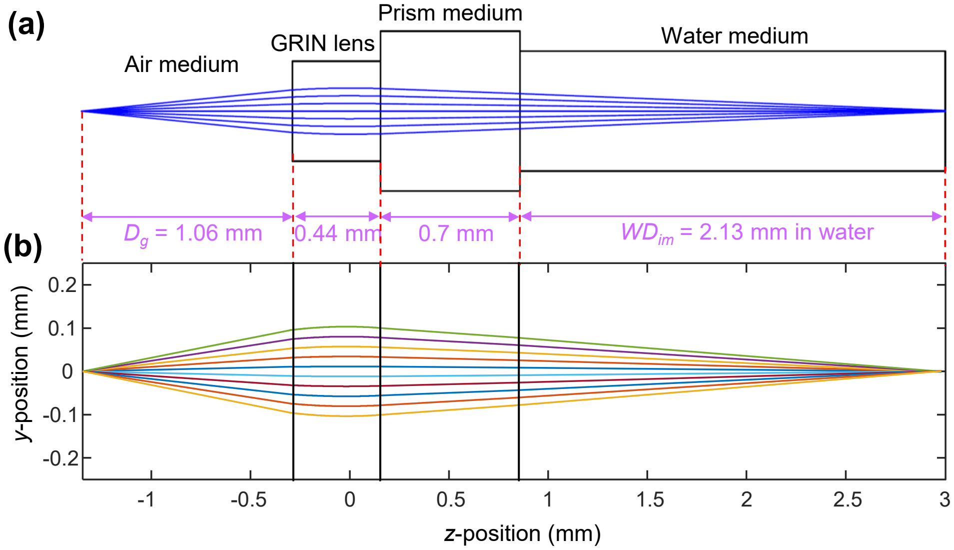

Fig. 4. Ray tracing results obtained by (a) the GRIN lens manufacturer using commercial optical design software and (b) us using the MATLAB code (Code 1) developed based on our ray tracing model. In both cases, the parameter values listed in Table 2 were applied. For our simulation, 10 rays were launched with initial angles (θ_1) ranging from 0 to the optical numerical aperture of the fiber (i.e., 0.1 in the simulation); however, of the 10 rays launched in the simulation, trajectory results for only 5 rays were reflected in the upper half-plane plotting for clarity, and the lower half-plane graphs were just mirrored.

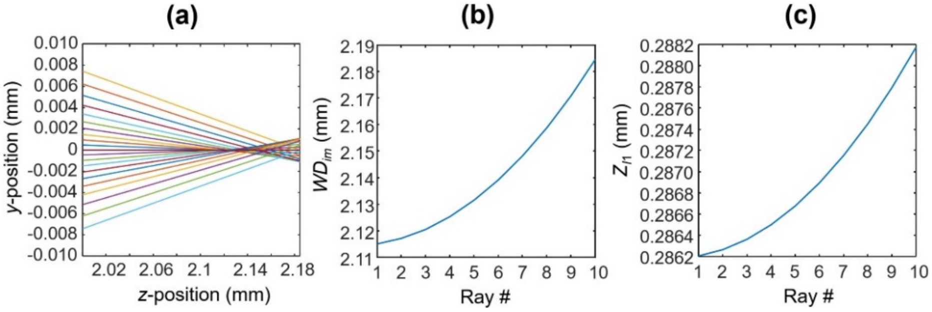

Fig. 5. (a) Magnified view of the focal zone from the ray tracing diagram shown in Fig. 4(b), calculated based on our model. (b) Working distance variations observed for the 10 launched rays. (c) Plot of Z_{I1} values, representing the physical length of the GRIN lens section over which each cosine ray ascends.

distance ($D_g = 1.06$ mm), and target working distance ($WD_{im} = 2.13$ mm) were defined by us. These values were selected based on the physical constraints of the mini-probe and the desired transverse resolution (i.e., numerical aperture). Based on these design inputs, the manufacturer determined the geometric length (Z_I) of the required GRIN lens to be 0.44 mm and produced the ray tracing output shown in Fig. 4(a). Accordingly, in our simulation [Fig. 4(b)], we used the parameter values listed in Table 2, including the finalized Z_I value of 0.44 mm, as well as g and n_0.

However, when we zoomed in on the focal zone of our ray tracing result presented in Fig. 4(b), we observed that the z-intercepts of individual rays exhibited slight deviations from the average focal distance (i.e., 2.13 mm), as shown in Fig. 5(a). Of course, some inaccuracies introduced by the paraxial approximation may also be present here, particularly for marginal rays. However, we primarily interpret these as a form of geometric aberration arising from the inclusion of multiple rays launched at varying angles in the simulation. In other words, although ideal ray tracing software would provide highly accurate tracing results without any errors caused by the paraxial approximation, the occurrence of a geometric aberration is inevitable under the assumed optical configuration [Fig. 2]. Referring to Figs. 5(a) and 5(b), it can be seen that rays fired at a relatively large angle form a focus at a longer distance.

As shown in Fig. 5(c), we also found that the calculated values of the variable Z_{I1} that represents the physical length of the GRIN lens segment over which a cosine ray ascends also varied by 2 µm rather than remain constant. When we first looked at these results, they seemed a bit puzzling because they contradicted the initial geometric assumption that the entrance surface of the GRIN lens must be flat. Fortunately, we realized that this outcome was a natural consequence of how we defined the Cartesian coordinate system—specifically by aligning the top of each cosine ray with the y-axis. That is, the observed variation in Z_{I1} occurred because we assumed the analytical solution of each ray for the paraxial ray equation [Eq. (3)] to the simple form of $a{\cdot}\cos(gz)$ rather than $a{\cdot}\cos[g(z-b)]$, where b denotes another constant. Thus, it can be understood that the location of the y-axis for each ray is being set differently during the calculation process—note that, nevertheless, all rays will move the same amount of displacement (i.e., Z_I) along the z-axis in the GRIN lens medium, and the only difference in the analytic solutions defining their individual trajectories is their amplitude a. Consequently, the variation in Z_{I1} should be understood as the peak position of each ray trajectory occurs at a different distance from the lens's entrance surface, and it is a limitation of the current model arises because we limited the analytic solutions of all ray trajectories to $a{\cdot}\cos(gz)$. In this regard, when running the code, one needs to be aware that an error may occur if the entire length of the GRIN lens (Z_I) is not set to be greater than the absolute values of the calculated Z_{I1}.

In plotting the ray tracing diagram shown in Fig. 4(b), to simplify the plotting code and reflect the flat entrance surface morphology, we applied artificial corrections to the calculated Z_{I1} values such that the surface distortion observed at the entrance of the GRIN lens is ignored (see Fig. 6, which shows a screen capture of the MATLAB code interface; see also line #49). Specifically, we adjusted the Z_{I1} values of all rays from the second to the last (i.e., indices 2 to Num_Ray) to match the Z_{I1} value of the first ray. Consequently, the corresponding Z_{I2} values were also recalculated to ensure that the sum of Z_{I1} and Z_{I2} remained equal to the constant total length Z_I (as shown in line #49).

When using the MATLAB code [Fig. 6], the launch angle (θ_1) of a ray from the optical fiber should be greater than zero but not exceed the numerical aperture of the optical fiber (NAfiber). Because the typical numerical aperture of optical fibers used in GRIN rod lens–based miniaturized imaging probes for biophotonics is approximately 0.1, and since this model is based on the paraxial approximation, it is essential to limit the maximum launch angle to this value. Additionally, the gap distance (D_g) must be set appropriately to ensure that the marginal ray remains within the maximum acceptance angle of the GRIN lens. As a general guideline, the y-coordinate of the marginal ray at the point of entry into the GRIN lens should be less than ~60% of the lens radius (i.e., $d/2$).

Although we only traced the trajectories of rays emitted upward from the fiber tip, as shown in Fig. 6, the trajectories of rays emitted downward can be easily obtained by mirroring the upward trajectories about the z-axis—see line #60. This approach was used to plot the full ray tracing diagram in Fig. 4(b).

This section demonstrated how the working distance (WD_{im}) can be predicted for a given geometrical length (Z_I) and the other parameters defined in the optical system [Fig. 3(b)].

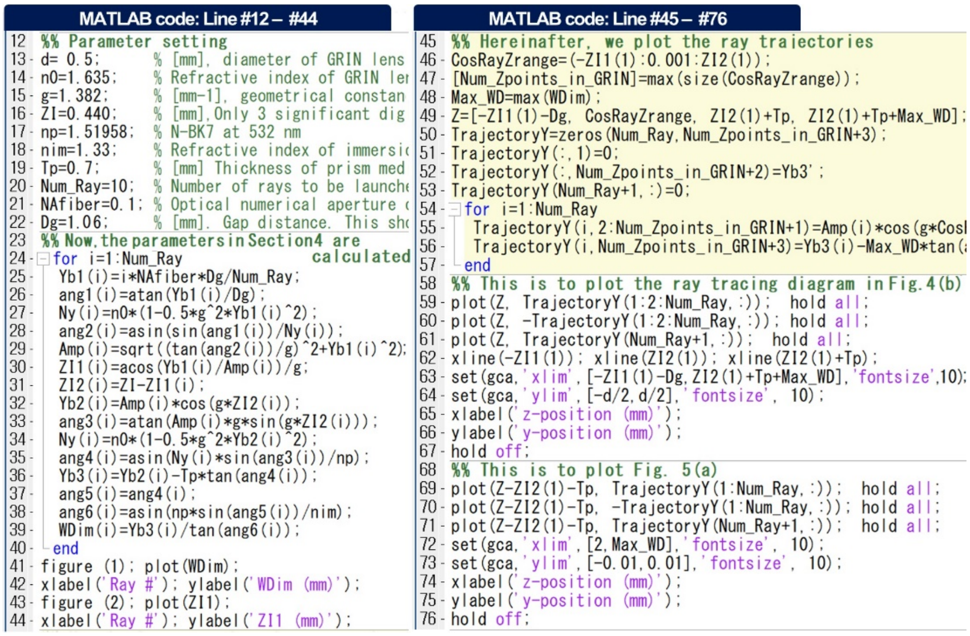

MATLAB code: Line #12 – #44

```
12   %% Parameter setting
13 - d= 0.5;        % [mm], diameter of GRIN lens
14 - n0=1.635;      % Refractive index of GRIN le
15 - g=1.382;       % [mm-1], geometrical constan
16 - ZI=0.440;      % [mm],Only 3 significant dig
17 - np=1.51958;    % N-BK7 at 532 nm
18 - nim=1.33;      % Refractive index of immersi
19 - Tp=0.7;        % [mm] Thickness of prism med
20 - Num_Ray=10;    % Number of rays to be launch
21 - NAfiber=0.1;   % Optical numerical aperture
22 - Dg=1.06;       % [mm]. Gap distance. This sh
23   %% Now,the parameters in Section4 are
24 - for i=1:Num_Ray                      calculated
25 -   Yb1(i)=i*NAfiber*Dg/Num_Ray;
26 -   ang1(i)=atan(Yb1(i)/Dg);
27 -   Ny(i)=n0*(1-0.5*g^2*Yb1(i)^2);
28 -   ang2(i)=asin(sin(ang1(i))/Ny(i));
29 -   Amp(i)=sqrt((tan(ang2(i))/g)^2+Yb1(i)^2);
30 -   ZI1(i)=acos(Yb1(i)/Amp(i))/g;
31 -   ZI2(i)=ZI-ZI1(i);
32 -   Yb2(i)=Amp(i)*cos(g*ZI2(i));
33 -   ang3(i)=atan(Amp(i)*g*sin(g*ZI2(i)));
34 -   Ny(i)=n0*(1-0.5*g^2*Yb2(i)^2);
35 -   ang4(i)=asin(Ny(i)*sin(ang3(i))/np);
36 -   Yb3(i)=Yb2(i)-Tp*tan(ang4(i));
37 -   ang5(i)=ang4(i);
38 -   ang6(i)=asin(np*sin(ang5(i))/nim);
39 -   WDim(i)=Yb3(i)/tan(ang6(i));
40 - end
41 - figure (1); plot(WDim);
42 - xlabel('Ray #'); ylabel('WDim (mm)');
43 - figure (2); plot(ZI1);
44 - xlabel('Ray #'); ylabel('ZI1 (mm)');
```

MATLAB code: Line #45 – #76

```
45   %% Hereinafter, we plot the ray trajectories
46 - CosRayZrange=(-ZI1(1):0.001:ZI2(1));
47 - [Num_Zpoints_in_GRIN]=max(size(CosRayZrange));
48 - Max_WD=max(WDim);
49 - Z=[-ZI1(1)-Dg, CosRayZrange, ZI2(1)+Tp, ZI2(1)+Tp+Max_WD];
50 - TrajectoryY=zeros(Num_Ray,Num_Zpoints_in_GRIN+3);
51 - TrajectoryY(:,1)=0;
52 - TrajectoryY(:,Num_Zpoints_in_GRIN+2)=Yb3';
53 - TrajectoryY(Num_Ray+1,:)=0;
54 - for i=1:Num_Ray
55 -   TrajectoryY(i,2:Num_Zpoints_in_GRIN+1)=Amp(i)*cos(g*Cos
56 -   TrajectoryY(i,Num_Zpoints_in_GRIN+3)=Yb3(i)-Max_WD*tan(
57 - end
58   %% This is to plot the ray tracing diagram in Fig.4(b)
59 - plot(Z, TrajectoryY(1:2:Num_Ray,:));  hold all;
60 - plot(Z, -TrajectoryY(1:2:Num_Ray,:)); hold all;
61 - plot(Z, TrajectoryY(Num_Ray+1,:));  hold all;
62 - xline(-ZI1(1)); xline(ZI2(1)); xline(ZI2(1)+Tp);
63 - set(gca,'xlim',[-ZI1(1)-Dg,ZI2(1)+Tp+Max_WD],'fontsize',10);
64 - set(gca,'ylim',[-d/2,d/2],'fontsize', 10);
65 - xlabel('z-position (mm)');
66 - ylabel('y-position (mm)');
67 - hold off;
68   %% This is to plot Fig. 5(a)
69 - plot(Z-ZI2(1)-Tp, TrajectoryY(1:Num_Ray,:));  hold all;
70 - plot(Z-ZI2(1)-Tp, -TrajectoryY(1:Num_Ray,:)); hold all;
71 - plot(Z-ZI2(1)-Tp, TrajectoryY(Num_Ray+1,:));  hold all;
72 - set(gca,'xlim',[2,Max_WD],'fontsize', 10);
73 - set(gca,'ylim',[-0.01,0.01],'fontsize', 10);
74 - xlabel('z-position (mm)');
75 - ylabel('y-position (mm)');
76 - hold off;
```

Fig. 6. Screen capture of the MATLAB code implemented based on the proposed ray tracing model (see Code 1).

Accordingly, by iteratively applying the forward prediction procedure, one can determine the final geometrical length (e.g., 0.44 mm) of the GRIN lens required for a given application.

6. Example of the imaging performance of the probe designed using this model

Based on the ray tracing results in Fig. 4, we finalized the GRIN lens geometry and optical layout, and placed an order with the manufacturer. However, upon receiving the customized GRIN lens, we discovered that the actual geometrical length was 0.40 mm—approximately 10% shorter than the target value of 0.44 mm, though still within the manufacturer's tolerance range. To maintain the original working distance ($WD_{im} = 2.13$ mm), we recalculated the gap distance (D_g) using our ray tracing model and updated it to 1.25 mm.

Figure 7 presents a photoacoustic endoscopic image of a rat colorectum acquired in vivo using the probe built with this configuration [Fig. 2(a)] and the updated parameters. Notably, the image reveals a honeycomb structure in the vasculature, suggesting a lateral resolution of approximately 10–13 µm—closely matching the initially predicted resolution of ~13 µm. This result serves as indirect evidence that our model can be reliably applied to real-world probe designs. Importantly, if the actual working distance of a probe deviates from the design due to implementation errors, the signal-to-noise ratio could significantly deteriorate because the laser focus would no longer coincide with the synthetic focal point of the dual ultrasonic transducers [Fig. 2(a)].

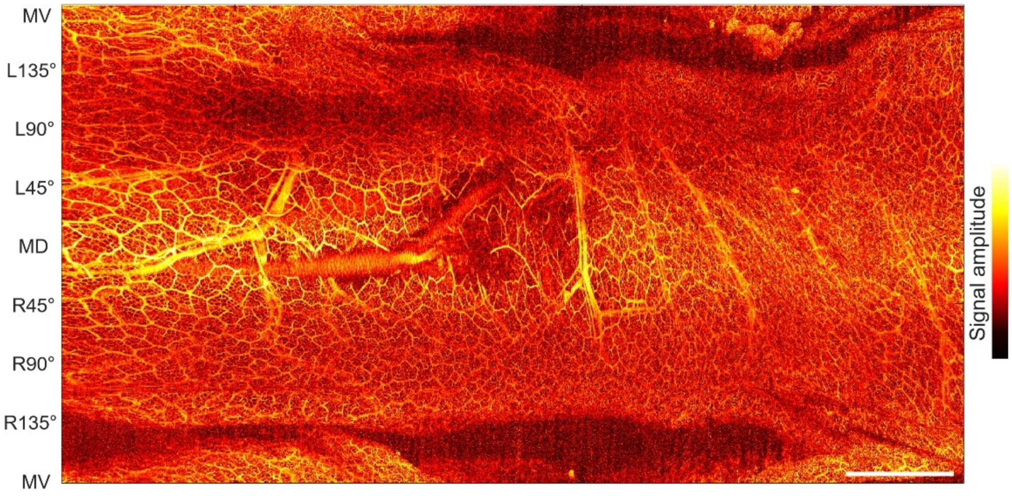

Fig. 7. Example of an in vivo photoacoustic endoscopic image acquired using the probe designed based on the proposed model. The image was obtained from a rat colorectum using the probe configured with the parameters listed in Table 2, except for the gap distance (D_g), which was adjusted to 1.25 mm as explained in the main text. The vertical axis corresponds to the angular FOV, covering 360°, and the scale bar represents a 5-mm range (horizontal axis only). MD, mid-dorsal; MV, mid-ventral; L, left; R, right.

7. Discussion

In this paper, we introduced our ray tracing model developed for designing GRIN lens–based miniaturized imaging probes and elaborated on both the foundational modeling concept and the utilization of the accompanying MATLAB code by demonstrating the procedure through which we arrived at the final design parameters for our photoacoustic endoscopic probes [21,22]. The central concept is that, under the assumption of paraxial ray theory, the trajectories of rays propagating through a GRIN lens medium must follow a sinusoidal path, as depicted in Fig. 1(b), and these analytic expressions can be completely determined by the boundary conditions set at the incident plane. This distinctive modeling approach applying that simple idea enables the trajectories of rays propagating through the various optical media presented in Fig. 2 to be expressed entirely in closed-form equations that can be calculated with minimal computational resources (the computation time for Fig. 4(b) using an Intel Core i7-4790 CPU @ 3.60 GHz was less than 0.5 seconds). We believe this feature offers a significant advantage, particularly for beginners, by providing a clearer understanding of the ray tracing mechanisms compared to commercial software, which typically produces only numerically derived results without offering deeper conceptual insights.

Due to space limitations, in Section 5, we presented only a single example of how to derive design parameters using our model, rather than providing a more extensive set of test results under varied conditions—such as the relationship between the working distance (WD_{im}) and the gap distance (D_g) at different pitch values or comparative analysis with commercial modeling tools like Zemax. However, for the first point, the relevant details are already comprehensively documented in Ref. 2. Regarding the second concern, as presented in Figs. S1–S5 of Supplement 1, we would like to note that in over five separate design cases—each involving different modeling parameters for other GRIN lens-based probes but sharing the same optical fiber–GRIN lens–right-angle prism configuration [Fig. 2], except for Fig. S4—the results of our model showed good agreement with those produced by the GRIN lens manufacturer using commercial optical design software: a difference of less than 80 µm between our results and the manufacturer's predictions was observed for the working distance. This consistent agreement has encouraged us to continue using our ray tracing code for the development of additional imaging probes with the same configuration assumed in Fig. 2, and to date, we have not encountered any significant issues.

However, when we applied our model to a different configuration—where a guiding optical fiber is placed in direct contact with a GRIN rod lens of much longer physical length (9.37 mm)—the working distance predicted by our model showed an increased error of up to approximately 180 µm compared to the 2 mm value predicted by Zemax (refer to Fig. S6 of Supplement 1). We interpret this as a natural result that could occur, because the larger the change in the y-coordinate of the ray, the more the simple cosine function approximation initially assumed deviates from the accurate trajectory. Nevertheless, since the optical configuration presented in Fig. 2(b) is a common design for miniaturized imaging probes in biophotonics, and because an optical fiber with a numerical aperture of approximately 0.1—where the paraxial approximation is valid—is typically used, we believe that our model provides a reasonable alternative for related simulations.

Upon reviewing the derivation process detailed in Section 4, it is clear that the only potential source of inaccuracy in our model lies in the approximation used for the GRIN lens medium, which is based on the paraxial ray assumption for the general ray equation [Eq. (1)]. Thus, if the y-value of the ray that travels in the GRIN lens medium shows a large variation within the medium, the model becomes inaccurate. Therefore, one may first need to consider whether this model can be applied in their own situation. Nevertheless, it is evident that the analytic solutions we have derived for other media regions—such as the prism and immersion layers—remain highly accurate because all of them were derived from fundamental Snell's law.

In this study, we developed a model that can predict the working distance of an imaging probe based on the mathematical derivation of the trajectories of paraxial rays originating from a single point on the optical axis. However, the model does not currently account for rays emerging from off-axis points or propagating along a helical trajectory in a GRIN lens medium. Moreover, even for the paraxial rays originating from a single point on the optical axis, this study did not present a concrete method for calculating other important parameters, such as the beam diameter and depth of focus at the focal zone, although there is a fundamental limitation in predicting the beam diameter itself, because it is rooted in ray optics—note that the ray distribution near the focal point, as shown in Fig. 5(a), is not a valid answer to this but mostly shows the results of geometric aberrations. While these limitations may not pose a significant problem—given that most optical fibers employed in miniaturized imaging probes for biophotonics are single-mode [1–12]—they could become more consequential in the case of other imaging probes that utilize a multimode optical fiber [Fig. 8], such as certain types of photoacoustic endoscopes [13–24]. For these systems, which apply a large-core multimode optical fiber, the lateral resolution is mostly governed by the beam diameter at the working distance; thus, our model may fall short in accurately predicting this parameter.

Nevertheless, even in such cases, it may still be possible to estimate the beam diameter using magnification, defined as the ratio of the image distance to the object distance—in a GRIN lens, these image and object distances are measured from the principal points, as defined in Fig. 1(d). For example, in the case of our photoacoustic endoscopic probe described in Section 3, the optical fiber had a core diameter of 10 µm, and the magnification factor calculated by our MATLAB code was approximately 1.3. Accordingly, a lateral resolution of about 13 µm can be expected, since the transverse plane where the rays converge corresponds to the image plane of the optical fiber tip. Although the core diameter exemplified here falls within a range that is somewhat ambiguous for applying this estimation, the magnification principle can still be appropriately applied to other optical fibers with much larger cores. Thus, unless a probe is designed with a magnification of less than one, using an optical fiber with a large core diameter offers limited benefit in enhancing lateral resolution, even though it allows for higher laser power delivery.

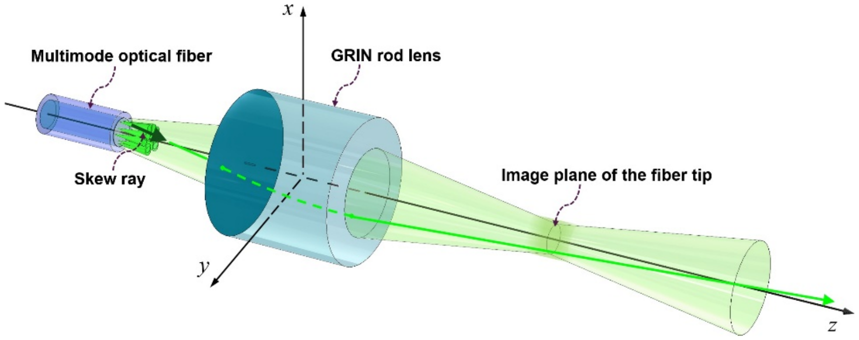

Fig. 8. Schematic showing a GRIN rod lens imaging probe involving a multimode optical fiber.

In Fig. 5, we see that the paraxial rays originating from a single point on the optical axis cannot be focused to a point after passing through the GRIN lens because of the geometric aberration. However, although we assume such an ideal case, in which no geometric aberration is involved, it is still impossible for all those rays to converge into a single point because of the diffraction nature of waves—of course, convergence of rays into a single point is possible in geometric optics by the assumptions of the related theory. Rather, the converging beam behaves like a Gaussian beam at or near the focal zone. Thus, if one knows the numerical aperture of the converging beam, it is possible to estimate the beam diameter at the focus and the depth of focus, or the Rayleigh range.

For example, if the magnification is assumed to be one, the numerical aperture of the converging beam will be the same as that of the beam emitted from the applied optical fiber (see Fig. 2). As the beam diameter and depth of focus are determined by the numerical aperture, it is possible to estimate these values and the lateral resolution eventually. Likewise, one can calculate those parameters for other magnifications (the greater the magnification, the larger the beam diameter at the working distance)—in fact, Ref. 2 offers more advantages in this regard because it was developed based on beam optics. That is, many other important parameters can be inferred based on the calculated working distance; for this reason, predicting the working distance has been the most important issue in related practices. In this respect, our model is valuable because it enables immediate visualization of ray trajectories and is thus expected to serve as a complementary tool alongside existing beam optics-based models [2,3] for the design of GRIN lens–based imaging probes.

Considering the length of this paper and the complexity of the corresponding MATLAB code, we modeled only the trajectories of the paraxial rays originating from a single point on the optical axis. However, if we extend the presented basic idea to more general cases involving skew rays, a more advanced analytic ray tracing model could be established—this model could also be applied to the multimode fiber case shown in Fig. 8. Although we still need to restrict the launch angle to a small value for the paraxial approximation in this case as well, it is possible to determine the analytic form of the ray propagating in the GRIN lens medium based on the boundary conditions, i.e., xy-coordinates and the direction vector at the incident point. As the general solution of the paraxial ray equation can be expressed by $y(z) = a{\cdot}\cos(gz) + b{\cdot}\sin(gz)$, where a and b represent the amplitudes of each term, the remaining task will be to determine these coefficient values by applying the boundary conditions (related knowledge is well established in Chapter 1 of Ref. 25). Of course, the same process applies to the x-trajectory.

For the optical system modeled in this study, we assumed a fiber–GRIN lens–prism configuration because it is one of the typical layouts adopted in many photoacoustic endoscopic probes [15,21,22]. However, other types of miniaturized imaging probes used in biomedical photoacoustics and related fields, such as optical coherence tomography and two-photon microscopy, often adopt a configuration without an air gap—that is, a guiding optical fiber is placed in direct contact with a GRIN rod lens as mentioned earlier. In this case, to achieve the required numerical aperture, a GRIN lens with a relatively smaller gradient constant and a longer pitch ($0.25 < P < 0.5$) than the case of the GRIN lens shown in Fig. 2 is applied—the configuration assumed for the simulation in Fig. S6 of Supplement 1 is a related example. In this configuration, as all rays start from the center of the entrance surface of the GRIN lens, the y-value (Yb1) at the interface should be set to 0, and the angle of refraction θ_2 (ang2) at the boundary can be directly set to a range from 0 to NAfiber/n0 in the MATLAB code rather than calculated using Eq. (2). A modified simulation code for this case is provided in Code 2 [52].

Moreover, even if the prism section is omitted, and the medium in which the optical focus is formed is typically air rather than water, the ray tracing process can still be carried out using this model by simply adjusting the refractive index of the immersion medium to 1.0 and setting the prism thickness to zero. Therefore, we believe this model could also be extended to aid in the design of more integrated imaging catheters, such as those incorporating optical coherence tomography. As the universalization of resources becomes increasingly important in various areas of biophotonics [47–50], the proposed model may serve as a useful tool to accelerate related research.

Funding. Ulsan National Institute of Science and Technology (1.220027.01); Ministry of SMEs and Startups (RS-2023-00303400); Ministry of Science and ICT, South Korea (IITP-2023-RS-2023-00259676); Ministry of Science and ICT, South Korea (RS-2024-00423610).

Disclosures. The authors declare no conflicts of interest.

Data availability. Data underlying the results presented in this paper are not publicly available at this time but may be obtained from the authors upon reasonable request.

Supplemental document. See Supplement 1 for supporting content.

References

1. S. H. Yun, G. J. Tearney, B. J. Vakoc, *et al.*, "Comprehensive volumetric optical microscopy in vivo," Nat. Med. **12**(12), 1429–1433 (2006).
2. W. Jung, W. Benalcazar, A. Ahmad, *et al.*, "Numerical analysis of gradient index lens–based optical coherence tomography," J. Biomed. Opt. **15**(6), 066027 (2010).
3. D. Lorenser, X. Yang, and D. D. Sampson, "Accurate modeling and design of graded-Index fiber probes for optical coherence tomography using the beam propagation method," IEEE Photonics J **5**(2), 3900015 (2013).
4. K. K. Chu, C. Unglert, T. N. Ford, *et al.*, "In vivo imaging of airway cilia and mucus clearance with micro-optical coherence tomography," Biomed. Opt. Express **7**(7), 2494–2505 (2016).
5. S. Liang, A. Saidi, J. Jing, *et al.*, "Intravascular atherosclerotic imaging with combined fluorescence and optical coherence tomography probe based on a double-clad fiber combiner," J. Biomed. Opt. **17**(7), 0705011 (2012).
6. S. Balakrishnan and A. L. Oldenburg, "All-fiber probes for endoscopic optical coherence tomography of the large airways," Appl. Opt. **60**(22), 6385–6392 (2021).
7. J. K. Kim, W. M. Lee, P. Kim, *et al.*, "Fabrication and operation of GRIN probes for in vivo fluorescence cellular imaging of internal organs in small animals," Nat. Protoc. **7**(8), 1456–1469 (2012).
8. J. Ahn, K. Choe, T. Wang, *et al.*, "In vivo longitudinal cellular imaging of small intestine by side-view endomicroscopy," Biomed. Opt. Express **6**(10), 3963–3972 (2015).
9. C. Li, K. Li, J. Liu, *et al.*, "Design of a confocal dispersion objective lens based on the GRIN lens," Opt. Express **30**(24), 44290–44299 (2022).
10. R. P J. Barretto, T. H. Ko, J. C. Jung, *et al.*, "Time-lapse imaging of disease progression in deep brain areas using fluorescence microendoscopy," Nat. Med. **17**(2), 223–228 (2011).
11. T. Wang, Q. Li, P. Xiao, *et al.*, "Gradient index lens based combined two-photon microscopy and optical coherence tomography," Opt. Express **22**(11), 12962–12970 (2014).
12. G. Meng, Y. Liang, S. Sarsfield, *et al.*, "High-throughput synapse-resolving two-photon fluorescence microendoscopy for deep-brain volumetric imaging in vivo," eLife **8**, e40805 (2019).
13. Y. Yang, X. Li, T. Wang, *et al.*, "Integrated optical coherence tomography, ultrasound and photoacoustic imaging for ovarian tissue characterization," Biomed. Opt. Express **2**(9), 2551–2561 (2011).
14. X. Bai, X. Gong, W. Hau, *et al.*, "Intravascular optical-resolution photoacoustic tomography with a 1.1 mm diameter catheter," PLoS One **9**(3), e92463 (2014).
15. B. Dong, S. Chen, Z. Zhang, *et al.*, "Photoacoustic probe using a microring resonator ultrasonic sensor for endoscopic applications," Opt. Lett. **39**(15), 4372–4375 (2014).

16. X. Dai, H. Yang, T. Shan, *et al.*, "Miniature endoscope for multimodal imaging," ACS Photonics **4**(1), 174–180 (2017).
17. Y. Li, R. Lin, C. Liu, *et al.*, "In vivo photoacoustic/ultrasonic dual-modality endoscopy with a miniaturized full field-of-view catheter," J. Biophotonics **11**(10), e201800034 (2018).
18. Y. Li, Z. Zhu, J. C. Jing, *et al.*, "High-speed integrated endoscopic photoacoustic and ultrasound imaging system," IEEE J. Select. Topics Quantum Electron. **25**(1), 1–5 (2019).
19. G. Li, Z. Guo, and S.-L. Chen, "Miniature probe for forward-view wide-field optical-resolution photoacoustic endoscopy," IEEE Sens. J. **19**(3), 909–916 (2019).
20. J. Leng, J. Zhang, C. Li, *et al.*, "Multi-spectral intravascular photoacoustic/ultrasound/optical coherence tomography tri-modality system with a fully-integrated 0.9-mm full field-of-view catheter for plaque vulnerability imaging," Biomed. Opt. Express **12**(4), 1934–1946 (2021).
21. M. Kim, K. W. Lee, K. S. Kim, *et al.*, "Intra-instrument channel workable, optical-resolution photoacoustic and ultrasonic mini-probe system for gastrointestinal endoscopy," Photoacoustics **26**, 100346 (2022).
22. K. S. Kim, J. Y. Youm, E. H. Lee, *et al.*, "Tapered catheter-based transurethral photoacoustic and ultrasonic endoscopy of the urinary system," Opt. Express **30**(15), 26169–26181 (2022).
23. Y. Liang, W. Fu, Q. Li, *et al.*, "Optical-resolution functional gastrointestinal photoacoustic endoscopy based on optical heterodyne detection of ultrasound," Nat. Commun. **13**(1), 7604 (2022).
24. X. Wen, P. Lei, S. Huang, *et al.*, "High-fluence relay-based disposable photoacoustic-ultrasonic endoscopy for in vivo anatomical imaging of gastrointestinal tract," Photonics Res. **11**(1), 55–64 (2023).
25. B. E. A. Saleh and M. C. Teich, *Fundamentals of Photonics* (John Wiley & Sons, Inc., 1991).
26. Y. Nishidate, T. Nagata, S. Y. Morita, *et al.*, "Ray-tracing method for isotropic inhomogeneous refractive-index media from arbitrary discrete input," Appl. Opt. **50**(26), 5192–5199 (2011).
27. M. Bahrami and A. V. Goncharov, "Geometry-invariant gradient refractive index lens: analytical ray tracing," J. Biomed. Opt. **17**(5), 055001 (2012).
28. M. Bahrami and A. V. Goncharov, "Geometry-invariant GRIN lens: finite ray tracing," Opt. Express **22**(23), 27797–27810 (2014).
29. S. Horiuchi, S. Yoshida, and M. Yamamoto, "Fast GPU-based ray tracing in radial GRIN lenses," Appl. Opt. **53**(19), 4343–4348 (2014).
30. K. N. Schrader, S. R. Subia, J. W. Myre, *et al.*, "Ray tracing in a finite-element domain using nodal basis functions," Appl. Opt. **53**(24), F10–20 (2014).
31. H.-Y. Tseng, Y.-B. Hong, C.-Y. Wu, *et al.*, "Monte Carlo simulation of radiative transfer in a medium with varying refractive index specified at discrete points," Appl. Math. Model. **48**, 870–884 (2017).
32. H. Ohno, "Symplectic ray tracing based on Hamiltonian optics in gradient-index media," J. Opt. Soc. Am. A **37**(3), 411–416 (2020).
33. Q. Zhang, Y. Tan, G. Ren, *et al.*, "Ray tracing method of gradient refractive index medium based on refractive index step," Appl. Sci. **11**(3), 912 (2021).
34. J. E. Gómez-Correa, "Geometrical-light-propagation in non-normalized symmetric gradient-index media," Opt. Express **30**(19), 33896–33910 (2022).
35. J. Shao, K. Zhu, X. Liu, *et al.*, "A general Monte Carlo method for polarized radiative transfer in multi-dimensional graded-index media," J. Quant. Spectrosc. Radiat. Transfer **278**, 108041 (2022).
36. M. Balasubramanian, S. D. Campbell, and D. H. Werner, "Sequential differential ray tracing formulation for homogeneous and gradient-index lenses using automatic differentiation," Opt. Eng. **62**(02), 021009 (2023).
37. H. Ohno and T. Usui, "Design method of gradient-index optics in homogeneous medium using neural network gradient-index mapping," Opt. Rev. **30**(3), 355–360 (2023).
38. W. Liu, Y. Ren, and F. Liu, "Analytical ray tracing based on Hamilton principal function and conjugate variable pairs," J. Opt. Soc. Am. A **40**(1), 78–84 (2023).
39. S. Horiuchi, S. Yoshida, and M. Yamamoto, "Numerical ray tracing method for an eccentric radial gradient-index rod lens," J. Opt. Soc. Am. A **31**(10), 2131–2134 (2014).
40. K. Tsukada and E. Nihei, "Ray tracing method in arbitrarily shaped radial graded-index waveguide," Appl. Opt. **54**(29), 8795–8799 (2015).
41. W. Liu, "Ray tracing in concentric gradient-index media: optical Binet equation," J. Opt. Soc. Am. A **39**(6), 1025–1033 (2022).
42. C. Yu, Y. Zong, M. Duan, *et al.*, "Adaptive ray tracing in freeform gradient-index media using an index directional derivative," Opt. Lett. **49**(19), 5375–5378 (2024).
43. B. McKeon and A. V. Goncharov, "Symplectic numerical methods in optics and imaging: ray tracing in spherical gradient-index lenses and computer-generated image rendering," Appl. Opt. **62**(32), 8621–8631 (2023).
44. W. Hu, C. M. C. Martin, and D. Cavallo, "Design formulas for flat gradient index lenses with planar or spherical output wavefront," IEEE Trans. Antennas Propagat. **72**(3), 2555–2563 (2024).
45. C. Flynn and A. V. Goncharov, "Semi-analytical finite ray-tracing through the quadratic symmetric GRIN lens," Appl. Opt. **63**(1), 290–298 (2024).
46. H. Ohno and T. Usui, "Points-connecting neural network ray tracing," Opt. Lett. **46**(17), 4116–4119 (2021).
47. M. Erfanzadeh and Q. Zhu, "Photoacoustic imaging with low-cost sources; A review," Photoacoustics **14**, 1–11 (2019).

48. A. Fatima, K. Kratkiewicz, R. Manwar, *et al.*, “Review of cost reduction methods in photoacoustic computed tomography,” Photoacoustics **15**, 100137 (2019).
49. T. Pan, D. Lu, H. Xin, *et al.*, “Biophotonic probes for bio-detection and imaging,” Light:Sci. Appl. **10**(1), 124 (2021).
50. K. C. Lee, K. Lee, J. Jung, *et al.*, “A smartphone-based Fourier ptychographic microscope using the display screen for illumination,” ACS Photonics **8**(5), 1307–1315 (2021).
51. J. Y. Youm and J. M. Yang, “Matlab codes utilized to trace the ray trajectories presented in Fig. 4(b),” figshare (2025), https://doi.org/10.6084/m9.figshare.29264171.
52. J. Y. Youm and J. M. Yang, “Matlab codes utilized to trace the ray trajectories presented in Fig. S6 of Supplement 1,” figshare (2025), https://doi.org/10.6084/m9.figshare.29264213.